

1 Chapter 14

XSW IMAGING

2 Michael J. Bedzyk

3 *Departments of Materials Science &*
4 *Engineering and Physics & Astronomy,*
5 *Northwestern University, 2220 Campus Dr.,*
6 *Evanston, IL 60208, USA*
7 *Argonne National Laboratory,*
8 *Argonne, IL 60439, USA*

9 Paul Fenter

10 *Chemical Sciences and Engineering Division,*
11 *Argonne National Laboratory, 9700 S.*
12 *Cass Avenue, Argonne, IL 60439, USA*

13 The summation of XSW measured hkl Fourier components is used to
14 generate a model-independent real-space map of an XRF-selected atomic
15 distribution. As a demonstration, this Fourier inversion method is used
16 to generate a set of 1D maps for a set of naturally occurring impurity
17 ions within a mica crystal and a 3D map for adsorbed Sn atoms on a
18 Ge(111) single crystal surface.

19 14.1. Introduction

20 In the most general sense, XSW probes the partial element-specific
21 geometrical structure factor, \mathcal{F}_H (in both amplitude and phase), in or above
22 a crystal. As already explained in Chapter 1, f_H is the amplitude (also
23 known as the coherent fraction) and P_H is the phase (also known as the
24 coherent position) of the H th-order Fourier coefficient of the normalized
25 distribution function^{1,2}:

$$26 \quad \mathcal{F}_H = \int \rho(\mathbf{r}) \exp(2\pi i \mathbf{H} \cdot \mathbf{r}) d\mathbf{r} = f_H \exp(2\pi i P_H). \quad (14.1)$$

2 *The X-ray Standing Wave Technique: Principles and Applications*

1 The phase sensitivity of XSW derives from the fact that the detector of the
 2 *E*-field is the fluorescent atom itself, lying within the “near-field” where
 3 the X-ray fields coherently interfere. (This is in contrast to conventional
 4 diffraction measurements; where the structure factor phase is lost because
 5 the scattered intensity is detected in the far-field.)

6 XSW can therefore be used directly to reconstruct the direct-space
 7 structure from a set of Fourier coefficients collected in reciprocal space.
 8 Based on the Fourier inversion of Eq. (14.1), the full time-averaged direct-
 9 space distribution of the atomic-centers, $\rho(\mathbf{r})$, of each fluorescent atomic
 10 species can be synthesized by the discrete Fourier summation^{3,4}:

$$\begin{aligned}\rho(\mathbf{r}) &= \sum_{\mathbf{H}} \rho_{\mathbf{H}} = \sum_{\mathbf{H}} f_{\mathbf{H}} \exp[2\pi i(P_{\mathbf{H}} - \mathbf{H} \cdot \mathbf{r})] \\ &= 1 + 2 \sum_{\substack{\mathbf{H} \neq -\mathbf{H} \\ \mathbf{H} \neq 0}} f_{\mathbf{H}} \cos[2\pi(P_{\mathbf{H}} - \mathbf{H} \cdot \mathbf{r})]\end{aligned}\quad (14.2)$$

11 The above simplification to a summation of cosine terms makes use of
 12 $f_0 = 1$ and the symmetry relationship analogous to Friedel’s law that makes
 13 $f_{\mathbf{H}} = f_{-\mathbf{H}}$ and $P_{\mathbf{H}} = -P_{-\mathbf{H}}$. This reconstruction of direct-space profiles is
 14 referred to as XSW imaging. The images are obtained without any reference
 15 to model structures, thereby representing in direct-space the information
 16 obtained by measuring the fluorescent yield modulations within the range
 17 of Bragg reflection.

18 Since the XSW phase is directly linked to the phase of the substrate
 19 electronic structure factor,⁵ the Bragg XSW positional information is
 20 acquired in the same absolute substrate unit cell coordinate system that
 21 was chosen when calculating the X-ray structure factors $F_{\mathbf{H}}$.

22 There are a number of ramifications that derive directly from the fact
 23 that the atomic density is determined by discrete Fourier synthesis as
 24 described in Eq. (14.2). In particular, the fidelity of the inverted image
 25 depends directly on the sampling frequency and the range over which
 26 the Fourier components are sampled. In the case of Bragg XSW, the
 27 sampling frequency in reciprocal space is limited to the discrete locations
 28 corresponding to allowed bulk Bragg reflections. Consequently, the image
 29 $\rho(\mathbf{r})$ generated from the XSW measured $f_{\mathbf{H}}$ and $P_{\mathbf{H}}$ values, is unique only
 30 in a volume corresponding to the primitive crystallographic unit cell of the
 31 bulk crystal; that is, the derived image is a projection of the full density
 32 profile into the unit cell. Consequently, the Bragg-XSW measurement is
 33 best-suited to probing structures that are localized over distances that are
 34 small with respect to the unit cell size, so that the full distribution can
 35 be determined uniquely. The range of reciprocal space over which the set

of \mathcal{F}_H values is measured determines the spatial resolution of the XSW image. This is evident when considering a one-dimensional reconstruction. The highest spatial frequency of the derived density profile corresponds to a period of $d_{H_{\max}} = 1/H_{\max}$. In particular, the phase sensitivity of XSW allows the two half-periods of the sinusoidal function to be distinguished directly, leading to an expected resolution of $\sim 1/2 d_{H_{\max}}$.

This approach is illustrated by simulating the Fourier synthesis of the diamond crystal structure along the 111 direction. As seen by the two vertical lines in Figs. 14.1(a) and 14.1(b), the 1D projection for this bilayer distribution can be represented by

$$\rho(z) = \frac{1}{2} \left[\delta\left(z + \frac{1}{8}\right) + \delta\left(z - \frac{1}{8}\right) \right], \quad (14.3)$$

where z is the 1D unit cell fractional coordinate relative to d_{111} . Using Eq. (14.1), the Fourier coefficient for this distribution is:

$$\mathcal{F}_{hhh} = \cos(\pi h/4), \quad (14.4)$$

which is plotted in Fig. 14.1(c). For this case the Fourier coefficient amplitudes are $f_{000} = f_{444} = f_{888} = 1$, $f_{111} = f_{333} = f_{555} = f_{777} = 1/\sqrt{2}$ and $f_{222} = f_{666} = 0$, and the phases are $P_{111} = P_{777} = P_{888} = 0$ and $P_{333} = P_{444} = P_{555} = 1/2$. In Fig. 14.1(a) the individual Fourier components ρ_{hhh} are plotted for $h = 0$ to 8 and then summed according to Eq. (14.2) to produce the 1D image in Fig. 14.1(b). This simple example provides the essential characteristics of the imaging process by discrete Fourier synthesis.

The location of the two halves of the diamond lattice bilayer is clearly resolved in this reconstruction of the density profile, in spite of the fact that maximum of the H th contribution to the density does not in general coincide with the locations of the atomic planes. As expected, the resolution in the reconstructed profile (defined as the FWHM of a discrete feature) in a given $[hkl]$ direction is equivalent to one-half of the smallest d-spacing (corresponding to H_{\max}) that is included in the summation. In the example, this results in a spatial resolution of $(d_{111}/8)/2 \sim 0.2 \text{ \AA}$, or $\Delta z = 1/16$, as observed in Fig. 14.1(b). Extra oscillations in the reconstructed profile are due to truncating the Fourier sum (effectively assigning zero amplitude to all terms higher than $hhh = 888$) and will be present so long as the amplitude of the missing Fourier components is non-zero (that is, the actual profile is not “resolved” by the data, but instead has a width limited by H_{\max}). Once sufficient data are obtained so that the reconstructed profile is fully resolved by the data then the oscillations due to termination error

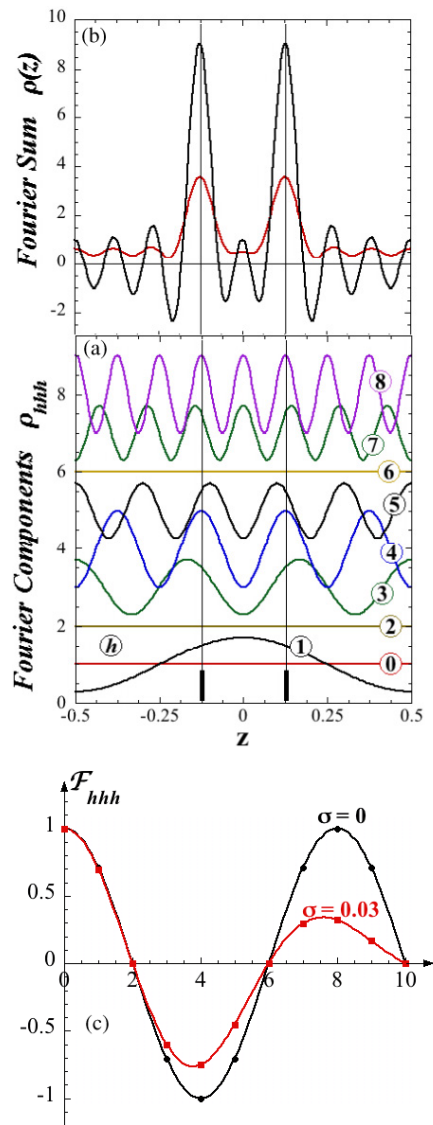


Fig. 14.1. (Continued)

Fig. 14.1. The 1D Fourier synthesis of the atoms crystallizing in the fcc diamond structure, e.g., Ge, along the 111 direction. (a) The 1D spatial-dependence of the $hh\bar{h}$ Fourier-components $\rho_{hh\bar{h}}, h = 0$ to 8, for the distribution of Ge atomic-centers in the diamond-cubic structure. Each curve is given a vertical offset of $+h$. The spatial interval corresponds to the 1D unit cell projected on the 111 direction and thus has a size corresponding to the d_{111} lattice spacing. There are two equally occupied Ge sites at $z = \pm 1/8$ (two vertical lines) based on Eq. (14.3). (b) The calculated 1D image $\rho(z)$ of the centers of the Ge atoms as summed over the terms from $hh\bar{h} = 000$ to 888 based on Eq. (14.2). Also shown (as a red line) is the case in which the two delta functions are replaced by two Gaussian functions with $\sigma = 0.03$. (c) The h dependence of the Fourier coefficients $F_{hh\bar{h}}$ for the two delta-function distribution (black line Eq. (14.4)) and two $\sigma = 0.03$ Gaussian function distribution (red line Eq. (14.6)). The curves in (a) can also be used to represent the phase and period of the XSW at the high-angle side ($\eta' < -1$) of the $hh\bar{h}$ Bragg peak for the case of $\Delta f'' = 0$.

1 are eliminated and the reconstructed profile closely resembles the intrinsic
2 profile.

3 This is illustrated in Fig. 14.1(b), where the curve with strong
4 oscillations was synthesized from the distribution defined by Eq. (14.3)
5 and the curve with damped oscillations was produced by the convolution
6 of this delta-function distribution with a normalized Gaussian function

$$G(z) = \frac{1}{\sqrt{2\pi}\sigma} \exp(-(\frac{z}{\sigma})^2/2) \quad (14.5)$$

7 with $\sigma = 0.03$ (FWHM = 0.071). This results in an increased width (0.094)
8 due to the convolution of the intrinsic width (0.071) and the resolution
9 width (0.063). Based on the convolution theorem the Fourier coefficients
10 for this Gaussian bilayer are

$$F_{hh\bar{h}} = \cos(\pi h/4) \exp(-2(\pi h\sigma)^2), \quad (14.6)$$

11 which is plotted in Fig. 14.1(c). This shows how the higher terms are
12 damped out. Inclusion of non-collinear Fourier components immediately
13 allows the 3D profile to be reconstructed.

14 This perspective of Fourier synthesis provides a clear demonstration
15 of the information content in an XSW data set. For example, the location
16 (i.e., the phase, indicated by P_{111}) of the wave maximum (see curve 1 in
17 Fig. 14.1(a)) corresponding to $\mathbf{H} = \overline{[111]}$ provides a direct measure of the
18 location of the average density, which is within the lattice bilayer. That
19 the density in the bilayer is distributed is revealed by the reduced coherent
20 fraction, f_{111} . There is, however, no direct (model-independent) information
21 concerning the precise locations of the sub-layers because these layers are

1 not resolved at $\mathbf{H} = \overline{[111]}$. Inclusion of additional Fourier components allows
2 the two sub-layers to be fully resolved in the reconstructed density image
3 at which point their locations can be directly determined by inspection.

4 One of the powerful characteristics of this approach is the ability to
5 use this model-independent information (with a typical spatial resolution
6 of $\sim 0.5 \text{ \AA}$) as both a model-independent starting point and as a conceptual
7 guide for subsequent model-dependent optimization (using parameters
8 to reproduce the measured coherent positions and fractions). This
9 substantially reduces the “guess work” involved in developing the final
10 structural model as long as a sufficient number of Fourier coefficients are
11 measured. This more standard model-dependent analysis method has a
12 typical structural sensitivity of $\sim 0.03 \text{ \AA}$.

13 This example also highlights an important subtlety of the XSW-
14 imaging method. Due to the diamond lattice structure, the structure factor
15 amplitude is zero for $\mathbf{H} = \overline{[222]}$ and $\overline{[666]}$ (i.e., these Bragg reflections are
16 “missing”). Since the reconstructed density profile need not have the same
17 symmetry as the diamond lattice (e.g., for surface adsorption profiles), the
18 absence of a Bragg reflection would mean that these Fourier components
19 cannot be measured and would be missing from the Fourier-reconstructed
20 profiles. This can lead to artifacts and consequently it is important that the
21 impact of the actual sampling of the Fourier components be kept in mind
22 in interpreting the reconstructed images.

23 14.2. 1D Profiling of Lattice Impurity Sites

24 The usefulness of this approach for directly revealing impurity site
25 distributions was first demonstrated through measurements of impurities in
26 muscovite (i.e., mica).³ Muscovite is a layered silicate with a tetrahedral-
27 octahedral-tetrahedral (TOT) sheet structure (with each sheet containing
28 tetrahedrally coordinated Si and Al in the T layers and octahedrally
29 coordinated Al in the O layer), with monovalent cations in the interlayer
30 between TOT sheets to provide charge-balance (Fig. 14.2). The distribution
31 of impurities (i.e., at <1%) cannot be determined directly by X-ray
32 crystallography since they have only a weak affect upon the total electron
33 density. While the local incorporation site might be obtained by EXAFS,
34 the ability of EXAFS to determine the local coordination geometry can be
35 limited when the element is found in multiple sites in a lattice. The use of
36 XSW to directly image the impurity distributions is illustrated in Fig. 14.2.

XSW Imaging

7

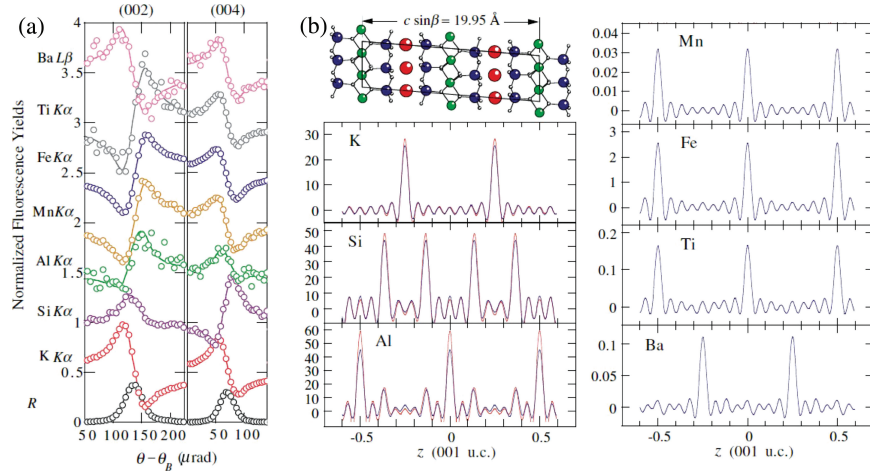


Fig. 14.2. Mica 1D ionic profiles: (a) Reflectivity and fluorescence modulations for the (002) and (004) reflections for both majority (Al, Si, K) and minority (Ba, Ti, Fe, Mn) elements in muscovite. (See Ref. 3 for the (006) to (0016) data and the measured values of f_H and P_H .) (b) The derived 1D density profiles obtained by discrete Fourier synthesis of the partial element structure factors as described in Eq. (14.2). The mica crystal structure is shown in (b) scaled so that the atom positions correspond directly with calculated profiles.

1 XSW data for numerous impurities (Mn, Fe, Ti, Ba) are obtained
 2 simultaneously through the use of an energy-dispersive XRF detector
 3 while exciting the muscovite Bragg reflections. The characteristic XSW
 4 modulation of the fluorescent yield is obtained in spite of the fact that
 5 muscovite crystals are non-ideal crystals (due to their tendency to bend).
 6 By illuminating just a tiny area of the surface with a $\sim 20\text{-}\mu\text{m}$ -sized X-ray
 7 beam with a relatively low photon energy of 7 keV, it was however possible
 8 to find regions of the crystal where the observed rocking curve width was
 9 close to the theoretical value.

10 The fluorescent modulation for each element was measured for $\mathbf{H} =$
 11 $[00L]$ with $L = 2$ through 16 for $L = \text{even}$ (due to the absence of odd-order
 12 reflections along $[00L]$). Results for $L = 2$ and 4 are shown in Fig. 14.2(a).
 13 These raw XSW data show that the fluorescent yield modulation for Ba
 14 follows that of K, while the modulation of Ti, Fe and Mn all follow the
 15 behavior of Al. Thus a traditional XSW analysis would conclude that Ba
 16 distribution is centered on the interlayer site, while the Ti, Fe and Mn would
 17 be centered on the octahedral site (the majority site for Al).

1 The derived model-independent elemental profiles obtained by Fourier
2 synthesis are shown in Fig. 14.2(b). Only reflections along [00*L*] were
3 measured since the height of a cation is sufficient to distinguish the various
4 lattice sites due to the layered nature of the muscovite structure. From
5 the synthesis of the impurity data in Fig. 14.2, it is immediately obvious
6 that Ba is found exclusively at the interlayer site, while Mn, Fe, and Ti are
7 all found in the octahedral site. This information is model-independent,
8 since only the total electron density of the muscovite crystal (i.e., that
9 determined by crystallography) was used in the dynamical X-ray scattering
10 theory calculations of the rocking curves. Also apparent from these model-
11 independent density distributions is a significant degree of “ringing” due to
12 an abrupt termination of the experimental data. This suggests that the
13 intrinsic distribution width of each element is narrow with respect to the
14 resolution width $d_{001}/16 = 1.2 \text{ \AA}$. These artifacts could be reduced through
15 the use of “Hanning” windows imposed on the measured coherent fractions,
16 but at some cost of resolution in the images.

17 Although the distribution of the major elements (Si, Al, K) is well
18 established by crystallography, these distributions were well reproduced by
19 the imaging approach showing that no significant artifacts are introduced
20 into the derived density profiles due to the discrete Fourier synthesis, as
21 seen by comparing to the derived profiles to that calculated using the known
22 crystal structure. These data confirm that Si is found only in the tetrahedral
23 site, K is only in the interlayer site, and Al is distributed between
24 tetrahedral and octahedral sites. Other elemental impurities in muscovite
25 (e.g., Na, Rb...) were not imaged either because the X-ray beam energy
26 was too low to excite measurable X-ray fluorescence, or the fluorescent X-
27 rays were too low in energy to be measured by the fluorescence detector.
28 Through measurement of the elemental composition (e.g., by X-ray
29 fluorescence), these data provide the site-specific composition of the crystal.

30 We note that it should be possible to obtain the individual profiles of
31 the major elements solely from these XSW data even if the crystal structure
32 were not known *a priori*. For instance, the K and Al distributions are out
33 phase for $L = 2$, but in phase for $L = 4$, with the Al distribution centered
34 on the origin and K displaced by $d_{001}/4$. The modulation amplitude of Al at
35 (004) is reduced with respect to that observed for K suggesting that the Al
36 is distributed unevenly between a majority site near the origin and minority
37 site separated by approximately $d_{001}/8$. In contrast, the (002) modulation
38 of Si has a fluorescence modulation corresponding to $f_{002} = 0$, suggesting
39 that there are two equally occupied Si sites displaced by $d_{001}/4$. The Si

site is displaced by $d/4$ with respect to the center of the Al distribution since its (004) fluorescence yield modulation is out of phase with respect to that for Al. By continuing along these lines and iterating with dynamical diffraction calculations, it therefore should be possible to determine the major element distributions within a crystal even when the crystal structure is unknown.

14.3. 3D Map of Surface Adsorbate Atoms

Having demonstrated that XSW imaging works for 1D profiling of impurity bulk lattice distributions,³ the method was extended to 3D mapping of adsorbate atoms and ions on single crystal surfaces. Cases included surfaces prepared by molecular-beam epitaxy,^{6,7} cation and anion adsorption from solution,^{8,9} atomic-layer deposition,¹⁰ and molecular self-assembly.¹¹

One of the UHV surfaces studied was 1/3 ML of Sn on Ge(111).⁶ This surface exhibits a $(\sqrt{3} \times \sqrt{3})R30^\circ$ to (3×3) reversible phase transition at $T_C \sim 210\text{ K}$.¹² For each of these two surface phases a 3D Sn atomic map was generated by the Eq. (14.2) summation of the (111), (333), (11 $\bar{1}$), and (33 $\bar{3}$) XSW measured Fourier components and their 3-fold symmetry equivalents. Figure 14.3 shows the image generated by the $\sqrt{3} \times \sqrt{3}$ room temperature XSW data. The top view is a cut at 2.0 Å above the top of the Ge bilayer and the side view is through the long diagonal of the (1×1) unit cell. In these images, the dark red represents the highest Sn density. The small black circles are added to indicate the bulk-terminated Ge atomic positions. The density oscillations that appear in the image are artifacts due to the truncation of the Fourier summation. This method projects the atomic distribution into the substrate (Ge) crystal primitive unit cell. Thus, if there are two distinct heights in the extended 2D superlattice, their projections will superimpose to form a combined distribution. (STM and/or SXRD are needed to extend beyond the 1×1 .) The resolution along the 111 direction corresponds to $1/2 d_{333} = 0.5\text{ \AA}$. Within this resolution, the Sn distribution shows an elongation along [111].

After refinement of the data (based on a T₄ site model), it was determined that two-thirds of the Sn are at 1.85(5) Å and one-third 0.45(5) Å higher. Comparing the XSW results above and below T_C confirmed a previously proposed dynamical fluctuation order-disorder phase transition for this corrugated 2D system.¹³

In general, this Fourier inversion method is of particular importance when a simple atomic position model cannot be easily found that is

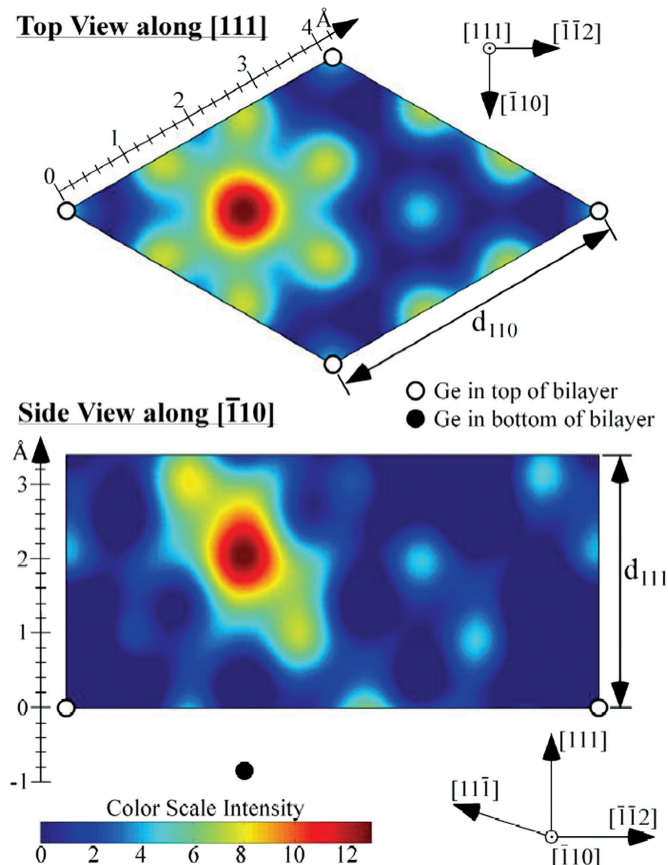


Fig. 14.3. 2D cuts through the maximum density of the 3D Sn atomic map generated by inserting XSW measured f_H and P_H into Eq. (14.2) for the $\sqrt{3} \times \sqrt{3}$ phase of 1/3 ML Sn/Ge(111). The top cut corresponds to the Ge(111) 1×1 surface unit cell. The Sn maximum is located laterally at the T₄ site, which is directly above the Ge atom in the bottom of the bilayer.

- ¹ consistent with the set of XSW measured Fourier components. This proved
- ² to be the case for a differently prepared 1/3 ML Sn/Ge(111) surface.
- ³ This surface, which was annealed at 573 K as opposed to 473 K for the
- ⁴ result shown in Fig. 14.3, produced a different set of Fourier coefficients
- ⁵ that generated an image with an unexpected (and unwanted) third Sn
- ⁶ position corresponding to Sn substituting for Ge in the bottom of the Ge
- ⁷ bilayer. Because this third Sn position lacked any long-range order, it was
- ⁸ undetectable by diffraction (LEED and SXRD).

As a general principle, XSW imaging (or Fourier inversion) is most powerful when used as the first stage in the XSW analysis process. After producing the model-independent $1/2$ -Å-resolution 3D atomic image, a model can then be proposed that is based on the image. This leads to the second XSW analysis stage corresponding to a χ^2 fit of a set of simultaneous equations in which each XSW measured hkl Fourier coefficient is equated to the corresponding parameterized coefficient from the model.

$$f_H \exp(2\pi i P_H) = \sum_j c_j \exp(i2\pi H \cdot \mathbf{r}_j) \exp(-2 < u_{H,j}^2 > d_H^{-2}) \quad (14.7)$$

The fit parameters are the coordinates \mathbf{r}_j , occupation fractions $c_j (\Sigma c_j = 1)$, and r.m.s. vibrational amplitudes ($< u_{H,j}^2 >^{1/2}$) for each of the model proposed sites.

14.4. Experimental Description

While a general description of the XSW instrumentation and procedures is discussed in Chapter 13, this Fourier inversion approach has some unique requirements with respect to its implementation. An experimental end-station used for these studies is shown as a photograph and schematic in Fig. 14.4 and further described in Refs. 14 and 15. The end-station uses two non-dispersive double-bounce silicon post-monochromators with a d-spacing typically chosen to closely match that of the selected Bragg planes of the sample. Each of the two rotational stages is equipped with a set of remotely selectable Si (hhh), ($hh0$), and ($00h$) channel-cut crystals. The incident beam channel-cut monochromators are used, either individually or in tandem, to tune the X-ray beam dispersion characteristics and optimize the measurement to best match the various Bragg reflections for the sample. More specifically, it is important to optimize the observed fluorescence modulation to improve the experimental sensitivity for measuring a particular Fourier coefficient. The capability of this type of setup to quickly change the λ versus θ emittance function of the post-monochromator for each reflection of the sample is important because the strength or weakness of a substrate Bragg reflection is, in general, unrelated to the importance of that Fourier component to the elemental density profile to be measured. Consequently, all symmetry inequivalent Fourier coefficients extending over the relevant reciprocal space volume should be measured to obtain an image.

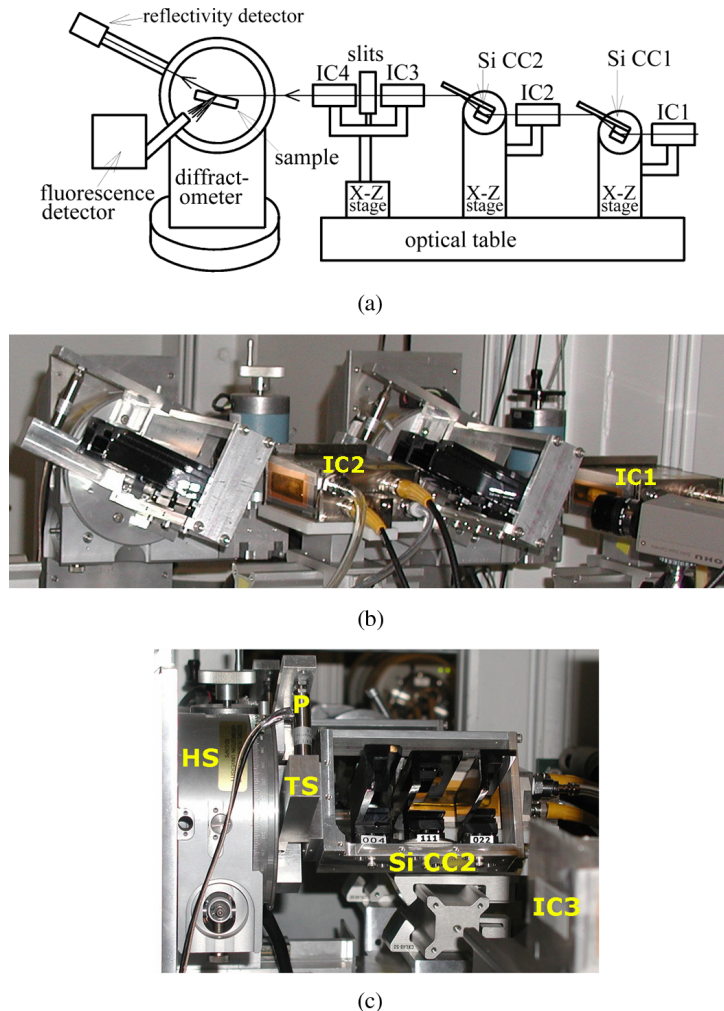


Fig. 14.4. Experimental system. (a) Side view schematic of the experimental components: four ion chambers (IC) monitor the X-ray flux after the beam is conditioned by the post-monochromator components. Two separate X - Z - θ stages manipulate Si channel-cut monochromators (Si CC1 and Si CC2) in the beam for the purpose of reducing the energy bandpass and angular divergence of the X-rays incident on the sample; (b) Side view image of the post-monochromator components. (c) Image showing up-stream view of the three channel-cut crystals mounted on a torsion-bearing stage (TS) attached to a Huber 410 rotary stage (HS). A piezo actuator (P) uses feedback from the ion chambers to maintain a fixed detuning value for the Si CC monochromators. The horizontal X translation stage at the base of each Si CC stage is used to select which of the three channel cuts intercepts the beam. Taken from Ref. 15.

14.5. Conclusion

As shown in this chapter, the Bragg XSW technique can be used to image the 3D real-space distribution of atoms in an element-specific and model-independent manner. Due to the limited set of allowed hkl Bragg reflections, the real-space information is limited to the spatial extent of the substrate unit cell. The XSW imaging technique has become a powerful tool especially with the availability of highly brilliant third-generation synchrotron sources. It is particularly well adapted to adsorbate systems, as shown here, or dopants within the unit cell of host lattices as demonstrated by the 1D imaging of naturally occurring trace impurities in mica³ or for 3D imaging of Mn doped GaAs.¹⁶ For nanocrystals grown on the surface of a single crystal substrate, XSW imaging can be used to measure the correlation between the two lattices, nanoparticle and substrate, revealing important parameters for describing the interfacial structure.¹⁷ As described in Chapters 5 and 19, the Fourier inversion of XSW data collected at the zeroth-order Bragg peak (or total external reflection) can be used to produce a model-independent 1D atomic density profile of the extended structure above a mirror surface^{18,19} with a lower-resolution, but longer length-scale; well beyond the reach of this single crystal Bragg XSW method.

Acknowledgments

Colleagues who contributed to the development and demonstration of these ideas include: Likwan Cheng, John Okasinski, Zhan Zhang, Chang-Yong Kim, Anthony Escudero, Jeffrey Catalano, Donald Walko, Denis Keane, and Neil Sturchio. The results in Figs. 14.2 and 14.3 were obtained at beamlines 12-ID-D and 5-ID-C, respectively, at the Advanced Photon Source, which is supported by the US Department of Energy. The work was also partially supported by the US National Science Foundation MRSEC Program and the Basic Energy Sciences Geoscience Research Program of the US Department of Energy.

References

1. N. Hertel, G. Materlik and J. Zegenhagen, *Z. Phys. B* **58** (1985) 199.
2. M. J. Bedzyk and G. Materlik, *Phys. Rev. B* **31** (1985) 4110.
3. L. Cheng, P. Fenter, M. J. Bedzyk and N. C. Sturchio, *Phys. Rev. Lett.* **90** (2003) 255503.
4. M. J. Bedzyk and L. W. Cheng, *Rev. Mineral Geochem.* **49** (2002) 221.
5. M. J. Bedzyk and G. Materlik, *Phys. Rev. B* **32** (1985) 6456.

6. J. S. Okasinski, C. Kim, D. A. Walko and M. J. Bedzyk, *Phys. Rev. B* **69** (2004) 041401.
 7. A. A. Escudero, D. M. Goodner, J. S. Okasinski and M. J. Bedzyk, *Phys. Rev. B* **70** (2004) 235416.
 8. Z. Zhang, P. Fenter, L. Cheng, N. C. Sturchio, M. J. Bedzyk, M. L. Machesky and D. J. Wesolowski, *Surf. Sci.* **554** (2004) L95.
 9. J. G. Catalano, Z. Zhang, P. Fenter and M. J. Bedzyk, *J. Colloid Interf. Sci.* **297** (2006) 665.
 10. C. Y. Kim, J. W. Elam, M. J. Pellin, D. K. Goswami, S. T. Christensen, M. C. Hersam, P. C. Stair and M. J. Bedzyk, *J. Phys. Chem. B* **110** (2006) 12616.
 11. R. Basu, J.-C. Lin, C.-Y. Kim, M. J. Schmitz, N. L. Yoder, J. A. Kellar, M. J. Bedzyk and M. C. Hersam, *Langmuir* **23** (2007) 1905.
 12. J. M. Carpinelli, H. H. Weiterring, M. Bartkowiak, R. Stumpf and E. W. Plummer, *Phys. Rev. Lett.* **79** (1997) 2859.
 13. J. Avila, A. Mascaraque, E. G. Michel, M. C. Asensio, G. LeLay, J. Ortega, R. Perez and F. Flores, *Phys. Rev. Lett.* **82** (1999) 442.
 14. D. A. Walko, O. Sakata, P. F. Lyman, T.-L. Lee, B. P. Tinkham, J. S. Okasinski, Z. Zhang and M. J. Bedzyk, *AIP Conf. Proc.* **705** (2004) 1166.
 15. M. J. Bedzyk, P. Fenter, Z. Zhang, L. Cheng, J. S. Okasinski and N. C. Sturchio, *Synchrotron Radiation News* **17** (2004) 5.
 16. T. L. Lee, C. Bihler, W. Schoch, W. Limmer, J. Daeubler, S. Thiess and J. Zegenhagen, *Phys. Rev. B* **81** (2010) 235202.
 17. Z. Feng, A. Kazimirov and M. J. Bedzyk, *ACS Nano* **5** (2011) 9755.
 18. M. J. Bedzyk, in *arXiv:0908.2115v1* (2009).
 19. V. Kohli, M. J. Bedzyk and P. Fenter, *Phys. Rev. B* **81** (2010) 054112.